Quantum disordered ground state in the triangular-lattice magnet NaRuO$_2$

Brenden R. Ortiz[1,8], Paul M. Sarte[1,8], Alon Hendler Avidor [1], Aurland Hay [1], Eric Kenney [2], Alexander I. Kolesnikov [3], Daniel M. Pajerowski[3], Adam A. Aczel [3], Keith M. Taddei[3], Craig M. Brown [4,5], Chennan Wang[6], Michael J. Graf [2], Ram Seshadri[1], Leon Balents[7] & Stephen D. Wilson [1] ✉

It has long been hoped that spin liquid states might be observed in materials that realize the triangular-lattice Hubbard model. However, weak spin–orbit coupling and other small perturbations often induce conventional spin freezing or magnetic ordering. Sufficiently strong spin–orbit coupling, however, can renormalize the electronic wavefunction and induce anisotropic exchange interactions that promote magnetic frustration. Here we show that the cooperative interplay of spin–orbit coupling and correlation effects in the triangular-lattice magnet NaRuO$_2$ produces an inherently fluctuating magnetic ground state. Despite the presence of a charge gap, we find that low-temperature spin excitations generate a metal-like term in the specific heat and a continuum of excitations in neutron scattering, reminiscent of spin liquid states previously found in triangular-lattice organic magnets. Further cooling produces a crossover into a different, highly disordered spin state whose dynamic spin autocorrelation function reflects persistent fluctuations. These findings establish NaRuO$_2$ as a cousin to organic, Heisenberg spin liquid compounds with a low-temperature crossover in quantum disorder.

The interplay between electron–electron correlation effects and geometrical frustration can lead to a rich hierarchy of electronic states. The Hubbard model at half-filling shows that as the on-site Coulomb interaction (U) is reduced relative to the electron hopping energy (t), the ground state transitions from an antiferromagnetic insulating state into a non-magnetic metal. If the underlying lattice is triangular, then an intermediate non-magnetic insulating state is predicted before the onset of the metallic state[1–3]. The predicted properties of this intermediate phase vary depending on the theoretical approach; however, it is generally envisioned as an inherently quantum disordered magnetic state or a quantum spin liquid phase generically realized at the boundary of the Mott insulating regime.

The proposed physical manifestations of this type of spin liquid state are rare, with well-studied candidates identified in anisotropic triangular magnets built from organic molecular complexes[4–7]. In inorganic compounds, however, triangular-lattice systems identified thus far are located either deep in the insulating regime[8], deep in the metallic state[9] or better described in the strong-coupling limit via a pure Heisenberg model[10]. One promising means of more fully exploring this materials space is to consider compounds with extended d electron orbitals, where the cooperative interplay between moderate on-site Coulomb repulsion (U) and spin–orbit coupling (λ)-driven bandwidth narrowing can generate marginally stable $J_{eff} = 1/2$ Mott insulating states with $U/t \approx 1$ (ref. 11). Such states are known to form in 5d transition metal
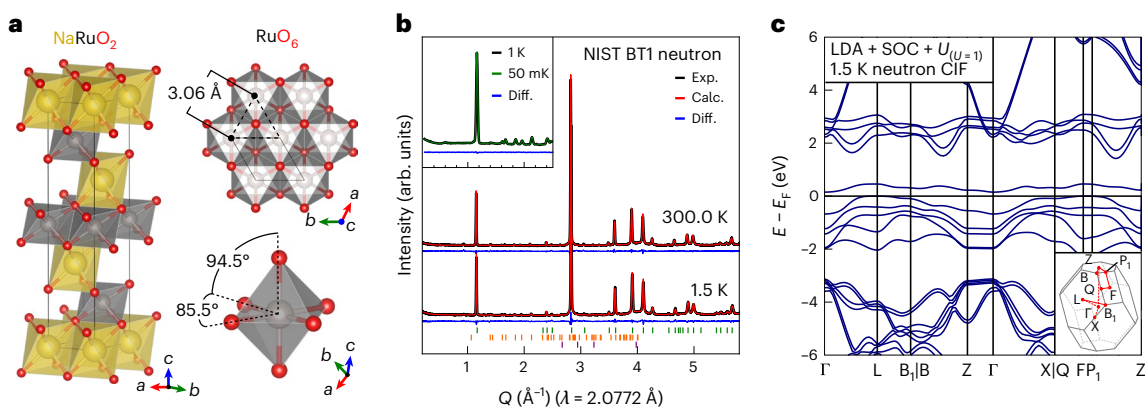
Fig. 1 | Lattice and electronic band structures of NaRuO$_2$. a, Crystal lattice of NaRuO$_2$ that forms in the $R3m$ space group, showing the triangular lattice of edge-sharing RuO$_6$ octahedra arranged in a layered structure separated by planes of Na ions. The slight trigonal distortion of the RuO$_6$ octahedra is illustrated. **b**, Neutron powder diffraction data collected at 300.0 K, 1.5 K, 1.0 K and 50 mK. Data in the main panel were collected at BT-1 and are overplotted with the refined structural diffraction pattern. The pattern includes NaRuO$_2$ (96.7% by weight) indexed by the top row of green ticks, Na$_2$CO$_3$ (2.9%) indexed with the middle row of orange ticks and Ru metal (0.4%) indexed with the bottom row of purple ticks. We note that powder samples prepared with higher-purity Na$_2$O$_2$ as the starting reagent do not show this small fraction of Na$_2$CO$_3$ impurity and exhibit the same properties as those reported here. The inset shows the data collected on HB-1A and reveals no magnetic scattering appearing down to 50 mK. The direct subtraction of the 1 K and 50 mK data is shown by the featureless blue line. **c**, LDA electronic band structure for NaRuO$_2$ using both λ and U = 1 eV. The inset shows the high-symmetry positions in the Brillouin zone.

iridates, where controlling the bandwidth can drive a metal–insulator transition[12], and similarly, weak J_{eff} = 1/2 Mott states may also be realized in 4d transition metal compounds[13].

Specifically, Ru^{3+} (4d^5) ions in a nearly ideal octahedral crystal field are capable of assuming a low-spin state, with both λ and U appreciable enough to stabilize a half-filled J_{eff} = 1/2 orbital[14,15]. An ideal triangular lattice consisting of octahedrally coordinated Ru^{3+} moments is also known to form in delafossite variants such as NaRuO$_2$ (ref. [16]), which suggests an opportune setting for searching for an intermediate quantum disordered state at the boundary of the J_{eff} = 1/2 Mott state's stability. Remarkably little is known regarding the ground state of this compound and, more generally, whether it can provide a suitable experimental window into the electronic properties of a near-critical triangular-lattice Hubbard model in the presence of strong λ.

Here we establish that NaRuO$_2$ hosts electrons in a unique interaction space as an ideal triangular lattice possessing a weak spin–orbit-assisted Mott insulating ground state—one consistent with the expectation of a near-critical J_{eff} = 1/2 Mott state driven by cooperative λ and U. Through studies of polycrystalline samples, our data demonstrate that despite the presence of a charge gap, the high-temperature magnetism of NaRuO$_2$ shows an elevated Pauli-like susceptibility, and at low temperatures where the charge gap is well established, heat capacity data show a substantial linear term akin to the Sommerfeld coefficients expected in metals. The magnetic excitations comprising this linear term generate a diffuse continuum of spin excitations, a portion of which is slowed down below a field-coupled crossover into a state with persistent fluctuations and a heat capacity quadratic in temperature. Our data demonstrate that J_{eff} = 1/2 electrons built from extended d orbitals on a triangular lattice stabilize quantum disordered magnetic-phase behaviour, consistent with expectations of Hubbard models near the metal–insulator phase boundary[17] as well as models of Kitaev antiferromagnets[18,19].

Figure 1a shows the detailed crystal structure of NaRuO$_2$. Edge-sharing RuO$_6$ octahedra form a triangular lattice of Ru^{3+} ions separated by planes of Na ions. An ideal equilateral triangle lattice results and a slight (<5°) trigonal distortion exists in the oxygen octahedra surrounding the Ru ions. Neutron diffraction data (Fig. 1b) show fully occupied Na and O sites and no site mixing with the resolution of the measurement. The predominant defect mode within NaRuO$_2$ is Na$_{Ru}$ antisite defect formation, which can be avoided by synthesizing

samples in a slightly Ru-rich environment[20]. Furthermore, neutron powder diffraction data collected at temperatures as low as 50 mK show no signs of structural symmetry breaking or static spin correlations forming between Ru moments. This is remarkable given the large covalency and enhanced exchange expected between the extended Ru moments, which are only 3.06 Å apart.

Ab initio electronic structure calculations (Fig. 1c) reveal that the band structure of NaRuO$_2$ is highly sensitive to the structural parameters. Using the experimentally derived structure in this paper, a charge gap forms via the inclusion of both λ and U using the local density approximation (LDA). Choosing U = 1 eV, consistent with prior LDA + λ + U models of Ru^{3+} systems such as RuCl$_3$ (ref. [21]), opens a gap when incorporated with λ. However, the model and prediction of the presence or absence of a gap is highly sensitive to the local distortions of oxygen octahedra around the Ru sites—consistent with the notion of a marginally insulating state where extended hopping effects can play an important role. The resistivity data (Fig. 2a) verify that NaRuO$_2$ indeed possesses an insulating ground state whose electrical transport is best modelled via two-dimensional variable-range hopping; however, we note that discrimination between two-dimensional and three-dimensional forms is difficult in polycrystalline samples. If the data above 200 K are parameterized by forcing an Arrhenius fit, the apparent gap value is $E_g \approx 0.22$ eV.

Contrasting the electrical transport data, the temperature-dependent magnetic susceptibility data (Fig. 2b) instead show a nearly itinerant magnetic response. The weak increase in the susceptibility on cooling does not fit to a conventional Curie–Weiss form; instead, the low-temperature susceptibility is best fit to a large Pauli-like term (χ_0) with a weak concentration of free impurity moments (1.8 ± 0.2% of S = 1/2 moments). The χ_0 term is unusually large for an insulator, namely, χ_0 = 9.6 ± 0.2 × 10^{-4} emu Oe^{-1} mol^{-1}, a value exceeding that of Pd metal with χ_0 = 7.3 × 10^{-4} emu Oe^{-1} mol^{-1} at 4 K (ref. [22]). As a consistency check, the large χ_0 fit via the temperature-dependent magnetization matches the linear term found in isothermal magnetization (χ_0 = 1.25 ± 0.10 × 10^{-3} emu Oe^{-1} mol^{-1}), which can be parameterized by a dominant Pauli-like linear term and a small fraction of S = 1/2 moments (1.4 ± 0.2%) (Fig. 2c). At lower temperatures, a weak cusp appears in the susceptibility data below 1.5 K (Fig. 2b, inset). There is a weak frequency dependence to the onset of this cusp (Supplementary Fig. 2), which deviates from the expectations of a canonical spin glass, but nevertheless suggests weak
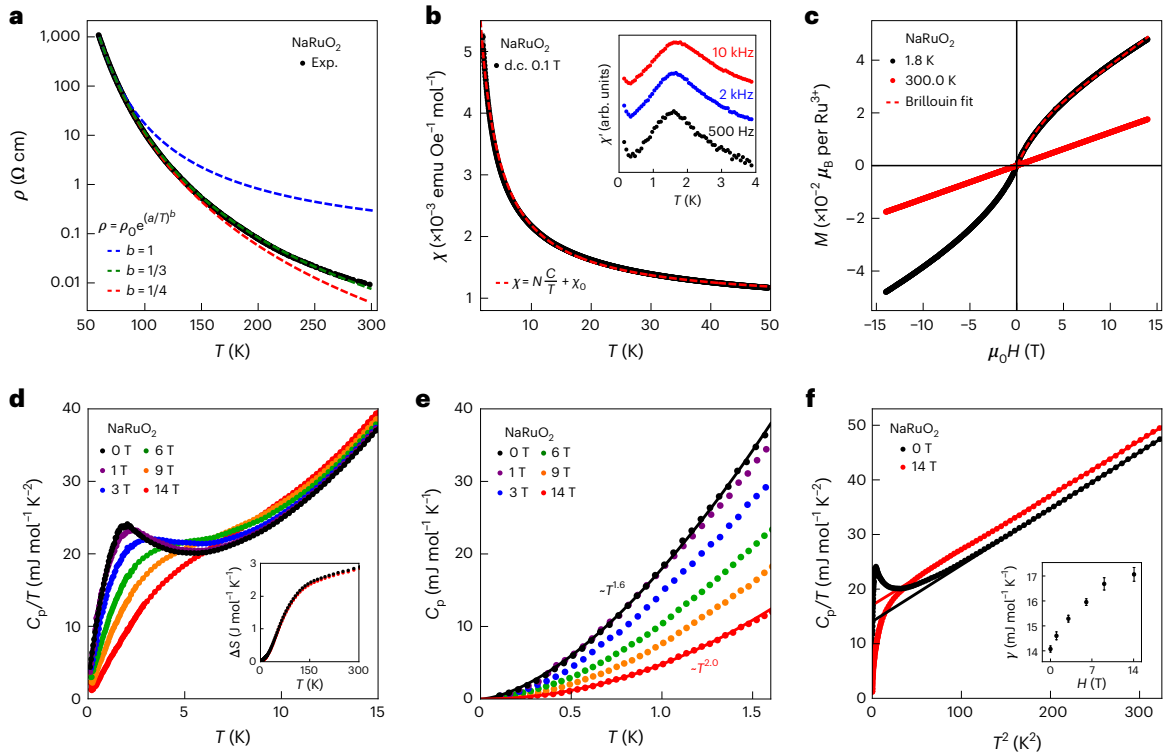
Fig. 2 | Electrical transport, magnetic susceptibility and heat capacity data characterizing the low-temperature properties of NaRuO$_2$. a, The d.c. resistivity data collected as a function of temperature. Fits to models of variable-range hopping transport are overplotted for both two-dimensional ($b = 1/3$) and three-dimensional ($b = 1/4$) forms, as well as fit to a conventional Arrhenius ($b = 1$) behaviour. **b**, Low-field magnetic susceptibility (M/H) collected under $\mu_0 H = 0.1$ T. The dashed line is a fit to a low-temperature Curie law with the addition of a substantial Pauli-like χ_0 term. The inset shows the magnetic susceptibility measured across the partial freezing transition near 1.5 K. For molar magnetic susceptibility, 1 emu Oe^{-1} mol^{-1} = $4\pi \times 10^{-6}$ m^3 mol^{-1}. **c**, Isothermal magnetization data collected at 1.8 K and 300.0 K. The dashed line shows a fit using a dominant, linear χ_0 term and $S = 1/2$ Brillouin function. **d**, Isobaric heat capacity $C_p(T)$ collected under a variety of magnetic fields. The inset shows the magnetic entropy extracted via the removal of the non-magnetic analogue NaRhO$_2$. **e**, Low-temperature heat capacity collected below the crossover at 1.5 K. Power-law fits are shown as the solid lines. **f**, $C_p(T)/T$ plotted as a function of T^2. The solid lines are fits to the model described in the main text. The inset shows the evolution of the effective Sommerfeld coefficients under the application of a magnetic field. The error bars represent one standard deviation in the parameter derived from a nonlinear least squares fit to the data.

freezing in the local moment contribution to the overall susceptibility. The nature of this slowdown in the dynamics is discussed later.

Exploring this further, the heat capacity data were collected down to 80 mK and are plotted in Fig. 2d. As the system is cooled far below the Debye temperature, $C_p(T)$ takes on the form $C_p(T) = \gamma T + \beta T^3$, where β parameterizes the contribution from phonons and γ is an anomalous linear term typically observed in metals. In free-electron gases, γ represents the Sommerfeld coefficient—a term proportional to the electronic density of states occupied at the Fermi level; however, in magnetically frustrated insulators, the presence of a γ term suggests a fractionalization of electrons and the presence of a spinon Fermi surface. The γ term in NaRuO$_2$ is substantial (14.07 ± 0.12 mJ mole^{-1} K^{-2}) and is distinct from the small γ values found in disordered insulators such as TiO$_2$ (0.1 mJ mole^{-1} K^{-1}) (refs. 23,24). Instead, it is comparable in magnitude with those found in organic triangular-lattice spin liquid candidates[25,26]. One notable distinction is that the presence of strong spin–orbit coupling amplifies χ_0 and the resulting Wilson ratio $R_W = \frac{\pi^2 k_B^2 \chi_0}{3 \mu_B^2 \gamma} = 8$ for NaRuO$_2$ versus $R_W \approx 1$ for organic compounds.

Cooling below 2 K reveals the onset of a weak freezing transition in $C_p(T)$ matching the cusp in the low-T susceptibility. Only a small amount of entropy is associated with this $T_F = 2$ K crossover ($1.2 \pm 0.2\%$ of $R\ln(2)$), further correlating it with the freezing of a small fraction of local moments. However, T_F also marks the onset of a modified power-law behaviour $C_p(T) = A T^\alpha$ that depends on the magnetic field. Applying a magnetic field shifts this T_F crossover upwards in temperature, and,

as the shoulder of this freezing feature shifts to higher temperatures, the low-temperature $C_p(T)$ converges to a quadratic behaviour ($\alpha = 2$). The application of a magnetic field also enhances the apparent γ term above T_F, and it increases by 21% under $\mu_0 H = 14$ T. We note that the magnetic entropy estimate (Fig. 2d, inset) becomes increasingly unreliable at higher temperatures due to an imperfect subtraction of the lattice contribution in the regime where magnetic fluctuations become substantially weaker compared with the phonon contributions. This potentially generates the weakly non-saturating response.

To investigate the nature of magnetic excitations associated with these low-energy fluctuations, inelastic neutron scattering measurements were performed. As an initial survey, temperature-subtracted data (1.8–300.0 K) are plotted in Fig. 3a, where the magnetic spectral weight at low momentum transfers appears centred near 25 meV. Energy cuts (integrated over small momentum transfers Q) of unsubtracted data are plotted for both 1.8 K and 300.0 K datasets (Fig. 3b) and show a peak in scattering at 1.8 K that is broadened, diminished and shifted downwards in energy on warming to 300.0 K. A similar subtraction of the data for a lower incident energy is also shown in Fig. 3c. The momentum distribution of the resulting gapless, low-energy continuum is centred near 1.2 Å^{-1} (Fig. 3d).

The broad continuum is further investigated at lower incident energies and temperatures (250 mK) (Fig. 3e). Spin fluctuations are gapless down to 0.1 meV with the spectral weight centred at finite momentum near $\mathbf{Q} = 1.2$ Å^{-1} as well as along low angles, suggestive of fluctuations centred at $\mathbf{Q} = 0$. On warming to 12.0 K (across the 1.5 K
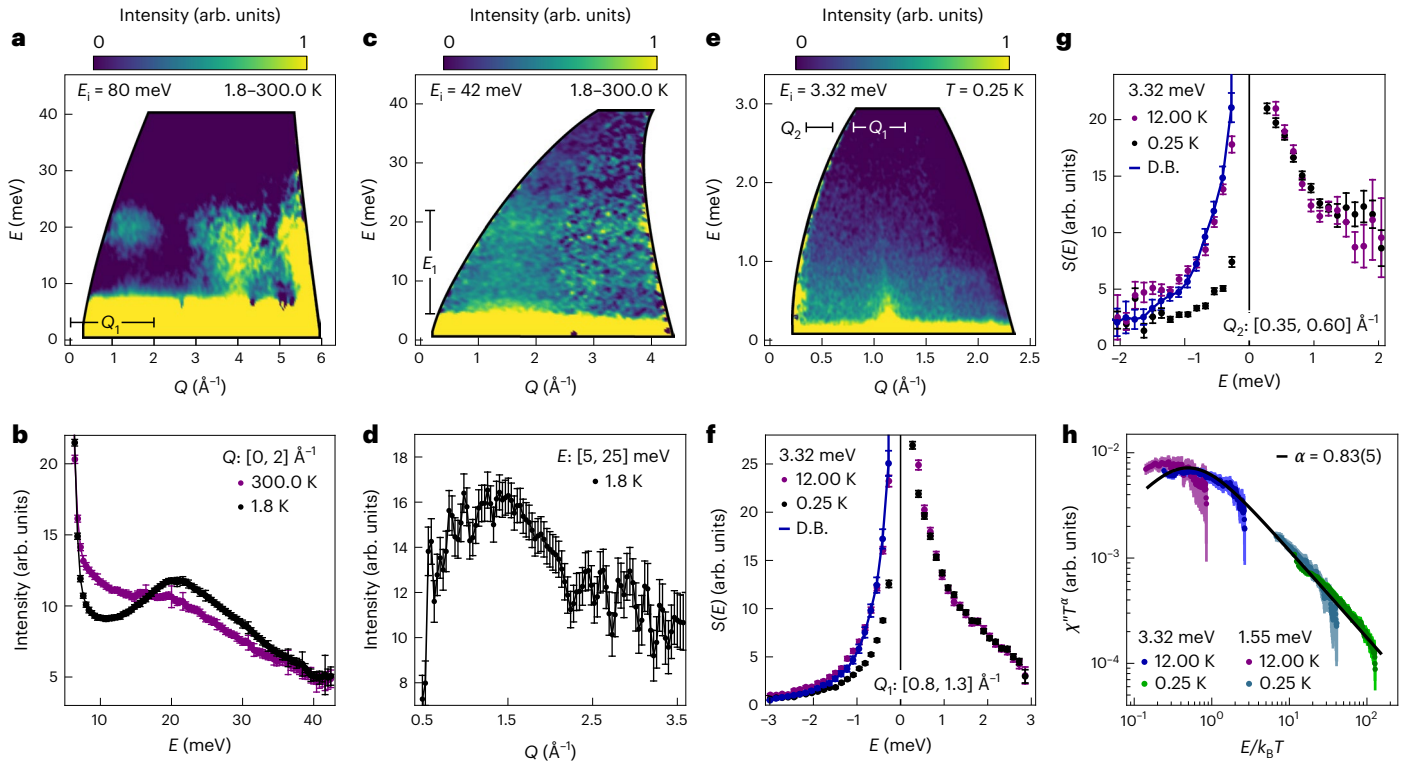
Fig. 3 | Inelastic neutron scattering data collected on NaRuO$_2$. a, Energy–momentum map of scattering intensity collected with $E_i = 80$ meV at 1.8 K with the 300.0 K data subtracted after correcting for the Bose population factor. **b**, Momentum-averaged energy cut through the temperature-subtracted map plotted in **a. c**, Energy–momentum map of scattering intensity collected with $E_i = 42$ meV at 1.8 K with the 300.0 K data subtracted after removing the Bose population factor. **d**, Energy-averaged momentum cut through the map plotted in **c. e**, Low-energy ($E_i = 3.32$ meV) energy–momentum map of scattering intensity collected at 1.8 K. **f,g**, Momentum-averaged energy cuts at 250 mK and 12 K collected at about 1.100 Å^{-1} (**f**) and 0.475 Å^{-1} (**g**) are plotted. The solid lines represent the expectation of scattering intensities at 12 K for $E < 0$ based on the detailed balance (D.B.) relation for excitations measured at 12 K with $E > 0$, where $S(Q, -E) = S(Q, E)e^{\frac{E}{k_B T}}$. **h**, Quantum critical scaling plot using momentum-averaged energy cuts about 1.1 Å^{-1} collected with $E_i = 3.32$ meV and $E_i = 1.55$ meV at various temperatures. Data were converted to $\chi''(Q, \omega)$ and scaled as described in the main text. The solid line represents the test scaling function described in the main text. The error bars in all the panels represent one standard deviation in the data based on Poissonian statistics with the sample size being the neutron counts.

cusp in $\chi'(T)$ and $C_p(T)$), these low-energy spin fluctuations are nearly temperature independent. Energy cuts through both finite momentum and low-angle spectral weights are shown in Fig. 3f,g, respectively. In both cases, excitations where the system gains energy ($E > 0$) are nearly temperature independent, whereas excitations where the system loses energy ($E < 0$) populate up with increasing temperature and follow a detailed balance. This behaviour in $S(Q, E)$ suggests quantum critical fluctuations in $\chi''(Q, E) = S(Q, E)(1 - e^{-E/k_B T})$ that potentially scale as a function of E/T. The low-energy data were tested for quantum critical scaling where $\chi''(Q, E)T^\alpha \propto f\left(\frac{E}{T}\right)$ by analysing collapse to a test function $\left(\frac{E}{T}\right) = \frac{\left(\frac{E}{T}\right)^\alpha}{\left(\frac{E}{T}\right)^{2\alpha} + \beta}$. Scaling collapse was optimized for $\alpha = 0.83 \pm 0.05$; although this test function is phenomenological, it reproduces the asymptotic $E/T \gg 1$ form of $f\left(\frac{E}{T}\right) \approx \left(\frac{E}{T}\right)^{-\alpha}$ expected in a number of quantum critical scaling relations[27,28]. The collapse of the data linked by this asymptotic form is consistent with robust quantum fluctuations present in the magnetic ground state of NaRuO$_2$.

To probe the spin dynamics at even lower frequencies, the muon spin relaxation technique was used for the determination of different static local fields and the presence of magnetic fluctuations. The temperature-dependent muon polarization and its fit are presented in Fig. 4a. At 12 K, the muon spin depolarization is best described via a Gaussian Kubo–Toyabe form dominated by the contribution of nuclear moments in the sample. On cooling below 12 K, the magnetic fluctuations from the antiferromagnetically coupled electronic spins slow down into the muon time window and the time-dependent polarization is described by a generalized depolarization function $P(t) = (f)_{GbG}(\Delta; R; t)e^{(-\lambda_{GbG}t)^\beta} + (1 - f)e^{-\lambda_p t}$. This is a response comprising an uncorrelated fraction $(1 - f)$ of paramagnetic moments whose fluctuations drive simple exponential relaxation at λ_p that, on cooling, converts into a highly disordered response captured by a Gaussian-broadened Gaussian (GbG) function supplemented by spin fluctuations in the form of a stretched exponential with relaxation rate λ_{GbG}. The GbG function[29] represents a normal distribution of Gaussian-field distributions about a central value Δ_0 with width w captured by the parameter $R = w/\Delta_0$. As shown in Fig. 4b, Δ_0 increases progressively with decreasing temperature below 3.0 K, and R becomes finite at approximately 2.5 K, with the value trending towards 1 at the base temperature. The absence of clear oscillatory signals suggests that the low-temperature state contains intermediate-diluted and disordered static magnetic moments. Meanwhile, this nominally static distribution of fields is modified by a slow fluctuation rate (λ_{GbG}) (Fig. 4c), similar to other highly frustrated materials with persistent spin fluctuations in their ground states[30]. To discriminate the presence of persistent fluctuations in this disordered ground state versus depolarization via static disorder, a longitudinal-field (LF) experiment was performed. Such a field rapidly decouples muons from slow depolarization due to purely static-field distributions, whereas depolarization persists in systems that are inherently dynamic[31]. The data in Fig. 4d indicate the persistence of fluctuations under modest applied fields, for example, contrasting the rapid decoupling seen in static-field
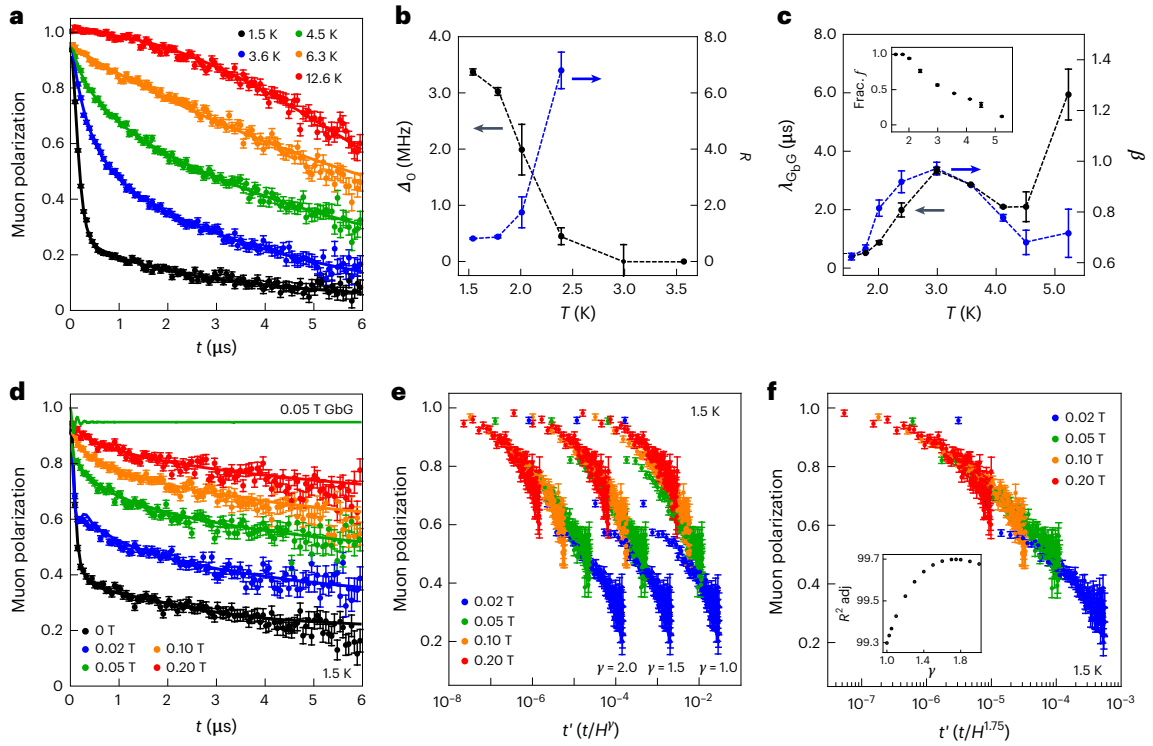
Fig. 4 | Muon spin relaxation data and analysis. a, Zero-field muon spin relaxation collected for a variety of temperatures. **b**,**c**, Fit values for the zero-field muon spin relaxation model described in the main text. **d**, Muon spin relaxation data collected at 1.5 K under a variety of applied LFs; the solid green curve is the calculated response for a fully static GbG function for the zero-field fit parameters and γ_{GbG} set to 0 at $T = 1.5$ K. The error bars represent one standard deviation of the data. **e**, The 1.5 K muon polarization under varying

LF strengths plotted with different exponents of t/H^γ. The error bars represent one standard deviation of the data. **f**, Scaling collapse of the 1.5 K LF data for an exponent of $\gamma = 1.75$. The inset shows the goodness of fit of the data to a third-order polynomial as a function of γ. The error bars in **a**, **d**, **e** and **f** represent one standard deviation in the data based on Poissonian statistics with the sample size being the muon counts. The error bars in **b** and **d** represent one standard deviation in the parameters derived from nonlinear least squares fits to the data.

distributions in frustrated yet statically frozen systems such as $Na_4Ir_3O_8$ (refs. [32,33]).

To further distinguish the partial freezing and persistent dynamics in $NaRuO_2$ from conventional spin-glass behaviour, we demonstrate the magnetic-field time-scaling relations of the LF time spectra using the form $P(H, t) = P(t/H^\gamma)$ (ref. [34]). The polarization maps to the spin autocorrelation function; above the freezing temperature, the depolarization should scale as a function of t/H^γ with the scaling exponent γ reflective of the manner through which spin correlations decay in time[35]. With the exception of the short-time-limit $\mu_0H = 0.02$ T data, the data scale well to this form with the analysis shown in Fig. 4e,f, and the R^2 value of the scaled data versus a test polynomial is shown in Fig. 4f (inset). This scaling analysis yields an exponent of $\gamma \approx 1.75$, which precludes conventional spin-glass power-law correlations ($\gamma \leq 1$) and, instead, is consistent with the expectation of decay via a stretched exponential function—identical to the type used to model the zero-field data.

The above experimental picture suggests that $NaRuO_2$ occupies a unique phase space where a spin–orbit-assisted Mott state gives rise to a native quantum disordered ground state. Charge fluctuations as well as anisotropic Kitaev interactions potentially play an important role in this disordered state. Ru^{3+} ions sit in an octahedral crystal field quantified by a quadratic elongation parameter[36] $\lambda_{quad} = 1.0074$, similar to that observed in Na_2IrO_3 (ref. [37]). This should promote the formation of a $J_{eff} = 1/2$ wavefunction from the t_{2g} orbital manifold. An array of such wavefunctions on a honeycomb lattice composed of edge-sharing octahedra generates strong Kitaev exchange and is predicted to stabilize a quantum spin liquid ground state, but experimental realizations are lacking. Although materials such as Na_2IrO_3 (ref. [38])

and $RuCl_3$ (ref. [39]) are known to stabilize strong ferromagnetic Kitaev coupling strengths, they nevertheless possess magnetically ordered ground states due to dominant Heisenberg interactions[40,41]. Similar predictions of dominant Kitaev exchange and quantum spin liquid phases have also been put forward for $J_{eff} = 1/2$ electrons decorating a triangular lattice[19]. However, unlike other Kitaev candidate materials, the thermodynamic phenomenology of $NaRuO_2$ resembles that of highly frustrated organic spin liquids and additional interactions such as charge fluctuations may play a role. We hypothesize that this is due to the weak nature of the insulating state and added the importance of longer-range exchange interactions. These ingredients are believed to stabilize intrinsically quantum disordered ground states[42,43] as we propose is realized here.

Inorganic compounds with simple structures and large-scale magnetic exchange energy rarely realize quantum disordered or spin-liquid-type ground states due to low-energy interactions, such as Dzyaloshinskii–Moriya interactions or weak lattice distortions that lift magnetic frustration. Even rarer is a quantum spin liquid candidate that manifests a transition/crossover between quantum disordered phases evident in the breakdown of the γ term in $NaRuO_2$. The unique interplay between the marginally insulating Mott state and anisotropic exchange fostered by cooperative spin–orbit coupling and on-site Coulomb interactions suggests that $NaRuO_2$ occupies a unique energy landscape—one where Kitaev coupling in the Hubbard model fosters nearby quantum disordered states. The result is a material that provides an appealing opportunity for pushing the manifestation of exotic phenomena such as non-Abelian quasiparticle excitations associated with a native spin liquid state up to higher temperatures for future quantum information applications.

Online content

Any methods, additional references, Nature Portfolio reporting summaries, source data, extended data, supplementary information, acknowledgements, peer review information; details of author contributions and competing interests; and statements of data and code availability are available at https://doi.org/10.1038/s41567-023-02039-x.

References

1. Morita, H., Watanabe, S. & Imada, M. Nonmagnetic insulating states near the Mott transitions on lattices with geometrical frustration and implications for κ-(ET)$_2$Cu$_2$(CN)$_3$. *J. Phys. Soc. Jpn* **71**, 2109–2112 (2002).
2. Sahebsara, P. & Senechal, D. Hubbard model on the triangular lattice: spiral order and spin liquid. *Phys. Rev. Lett.* **100**, 136402 (2008).
3. Laubach, M., Thomale, R., Platt, C., Hanke, W. & Li, G. Phase diagram of the Hubbard model on the anisotropic triangular lattice. *Phys. Rev. B* **91**, 245125 (2015).
4. Yamashita, S. et al. Thermodynamic properties of a spin-1/2 spin-liquid state in a κ-type organic salt. *Nat. Phys.* **4**, 459–462 (2008).
5. Isono, T. et al. Gapless quantum spin liquid in an organic spin-1/2 triangular-lattice κ−H$_3$(Cat-EDT-TTF)$_2$. *Phys. Rev. Lett.* **112**, 177201 (2014).
6. Itou, T., Oyamada, A., Maegawa, S., Tamura, M. & Kato, R. Quantum spin liquid in the spin-1/2 triangular antiferromagnet EtMe$_3$Sb[Pd(dmit)$_2$]$_2$. *Phys. Rev. B* **77**, 104413 (2008).
7. Shimizu, Y., Miyagawa, K., Kanoda, K., Maesato, M. & Saito, G. Spin liquid state in an organic Mott insulator with a triangular lattice. *Phys. Rev. Lett.* **91**, 107001 (2003).
8. Bordelon, M. M. et al. Field-tunable quantum disordered ground state in the triangular-lattice antiferromagnet NaYbO$_2$. *Nat. Phys.* **15**, 1058–1064 (2019).
9. Mackenzie, A. P. The properties of ultrapure delafossite metals. *Rep. Prog. Phys.* **80**, 032501 (2017).
10. Collins, M. F. & Petrenko, O. A. Review/Synthèse: triangular antiferromagnets. *Can. J. Phys.* **75**, 605–655 (1997).
11. Kim, B. J. et al. Novel J_{eff}=1/2 Mott state induced by relativistic spin-orbit coupling in Sr$_2$IrO$_4$. *Phys. Rev. Lett.* **101**, 076402 (2008).
12. Moon, S. J. et al. Dimensionality-controlled insulator-metal transition and correlated metallic state in 5d transition metal oxides Sr$_{n+1}$Ir$_n$O$_{3n+1}$ (n=1, 2, and ∞). *Phys. Rev. Lett.* **101**, 226402 (2008).
13. Plumb, K. W. et al. α-RuCl$_3$: a spin-orbit assisted Mott insulator on a honeycomb lattice. *Phys. Rev. B* **90**, 041112(R) (2014).
14. Yadav, R. et al. Kitaev exchange and field-induced quantum spin-liquid states in honeycomb α-RuCl$_3$. *Sci. Rep.* **6**, 37925 (2016).
15. Koitzsch, A. et al. J_{eff} description of the honeycomb Mott insulator α−RuCl$_3$. *Phys. Rev. Lett.* **117**, 126403 (2016).
16. Shikano, M., Delmas, C. & Darriet, J. NaRuO$_2$ and Na$_x$RuO$_{2y}$H$_2$O: new oxide and oxyhydrate with two dimensional RuO$_2$ layers. *Inorg. Chem.* **43**, 1214–1216 (2004).
17. Yang, H.-Y., Läuchli, A. M., Mila, F. & Schmidt, K. P. Effective spin model for the spin-liquid phase of the Hubbard model on the triangular lattice. *Phys. Rev. Lett.* **105**, 267204 (2010).
18. Kos, P. & Punk, M. Quantum spin liquid ground states of the Heisenberg-Kitaev model on the triangular lattice. *Phys. Rev. B* **95**, 024421 (2017).
19. Li, K., Yu, S.-L. & Li, J.-X. Global phase diagram, possible chiral spin liquid, and topological superconductivity in the triangular Kitaev–Heisenberg model. *New J. Phys.* **17**, 043032 (2015).
20. Ortiz, B. R., Sarte, P. M., Avidor, A. H. & Wilson, S. D. Defect control in the Heisenberg-Kitaev candidate material NaRuO$_2$. *Phys. Rev. Mater.* **6**, 104413 (2022).
21. Sinn, S. et al. Electronic structure of the Kitaev material α-RuCl$_3$ probed by photoemission and inverse photoemission spectroscopies. *Sci. Rep.* **6**, 39544 (2016).
22. Jamieson, H. C. & Manchester, F. D. The magnetic susceptibility of Pd, PdH and PdD between 4 and 300 K. *J. Phys. F: Met. Phys.* **2**, 323 (1972).
23. Smith, S. J. et al. Heat capacities and thermodynamic functions of TiO$_2$ anatase and rutile: analysis of phase stability. *Am. Mineral.* **94**, 236–243 (2009).
24. Schliesser, J. M. & Woodfield, B. F. Lattice vacancies responsible for the linear dependence of the low-temperature heat capacity of insulating materials. *Phys. Rev. B* **91**, 024109 (2015).
25. Ni, J. M. et al. Absence of magnetic thermal conductivity in the quantum spin liquid candidate EtMe$_3$Sb[Pd(dmit)$_2$]$_2$. *Phys. Rev. Lett.* **123**, 247204 (2019).
26. Yamashita, S., Yamamoto, T., Nakazawa, Y., Tamura, M. & Kato, R. Gapless spin liquid of an organic triangular compound evidenced by thermodynamic measurements. *Nat. Commun.* **2**, 275 (2011).
27. Schröder, A., Aeppli, G., Bucher, E., Ramazashvili, R. & Coleman, P. Scaling of magnetic fluctuations near a quantum phase transition. *Phys. Rev. Lett.* **80**, 5623 (1998).
28. Sachdev, S. & Ye, J. Universal quantum-critical dynamics of two-dimensional antiferromagnets. *Phys. Rev. Lett.* **69**, 2411 (1992).
29. Noakes, D. R. & Kalvius, G. M. Anomalous zero-field muon spin relaxation in highly disordered magnets. *Phys. Rev. B* **56**, 2352 (1997).
30. Hodges, J. A. et al. First-order transition in the spin dynamics of geometrically frustrated Yb$_2$Ti$_2$O$_7$. *Phys. Rev. Lett.* **88**, 077204 (2002).
31. Uemura, Y. J. et al. Spin fluctuations in frustrated kagomé lattice system SrCr$_8$Ga$_4$O$_{19}$ studied by muon spin relaxation. *Phys. Rev. Lett.* **73**, 3306 (1994).
32. Dally, R. et al. Short-range correlations in the magnetic ground state of Na$_4$Ir$_3$O$_8$. *Phys. Rev. Lett.* **113**, 247601 (2014).
33. Shockley, A. C., Bert, F., Orain, J. C., Okamoto, Y. & Mendels, P. Frozen state and spin liquid physics in Na$_4$Ir$_3$O$_8$: an NMR study. *Phys. Rev. Lett.* **115**, 047201 (2015).
34. Keren, A. Muons as probes of dynamical spin fluctuations: some new aspects. *J. Phys.: Condens. Matter* **16**, S4603 (2004).
35. Keren, A., Mendels, P., Campbell, I. A. & Lord, J. Probing the spin-spin dynamical autocorrelation function in a spin glass above T_g via muon spin relaxation. *Phys. Rev. B* **77**, 1386 (1996).
36. Robinson, K., Gibbs, G. V. & Ribbe, P. H. Quadratic elongation: a quantitative measure of distortion in coordination polyhedra. *Science* **172**, 567–570 (1971).
37. Ye, F. et al. Direct evidence of a zigzag spin-chain structure in the honeycomb lattice: a neutron and X-ray diffraction investigation of single-crystal Na$_2$IrO$_3$. *Phys. Rev. B* **85**, 180403(R) (2012).
38. Chun, S. H. et al. Direct evidence for dominant bond-directional interactions in a honeycomb lattice iridate Na$_2$IrO$_3$. *Nat. Phys.* **11**, 462–466 (2015).
39. Banerjee, A. et al. Neutron scattering in the proximate quantum spin liquid α-RuCl$_3$. *Science* **356**, 1055–1059 (2017).
40. Cao, H. B. et al. Low-temperature crystal and magnetic structure of α−RuCl$_3$. *Phys. Rev. B* **93**, 134423 (2016).
41. Ye, F. et al. Direct evidence of a zigzag spin-chain structure in the honeycomb lattice: a neutron and X-ray diffraction investigation of single-crystal Na$_2$IrO$_3$. *Phys. Rev. B* **85**, 180403 (2012).
42. Lee, S.-S. & Lee, P. A. U(1) gauge theory of the Hubbard model: spin liquid states and possible application to κ–(BEDT–TTF)$_2$Cu$_2$(CN)$_3$. *Phys. Rev. Lett.* **95**, 036403 (2005).
43. Motrunich, O. I. Variational study of triangular lattice spin-1/2 model with ring exchanges and spin liquid state in κ–(ET)$_2$Cu$_2$(CN)$_3$. *Phys. Rev. B* **72**, 045105 (2005).

Methods

Sample preparation

Polycrystalline $NaRuO_2$ was synthesized using mechanochemical methods. Sodium peroxide (Na_2O_2) beads (Sigma, 97.00%), ruthenium dioxide (RuO_2) powder (Alfa, 99.95%) and sodium metal (Alfa 99.8%) are combined in a pre-seasoned tungsten carbide ball-mill vial under argon. The synthesis generally needs excess Na and O during the reaction; however, we note that $NaRuO_2$ exhibits an unusually large degree of off-stoichiometry in the Na-rich regime. To optimize the purity and Na stoichiometry, we have designed the synthesis to minimize Na_{Ru} antisite defects by forcing $NaRuO_2$ to crystallize in equilibrium with Ru and $NaRu_2O_4$, which corresponds to the Ru-rich edge of the phase diagram. Thus, the stoichiometry has been empirically tuned to $Na_{1.07}(Na_2O_2)_{0.35}(RuO_2)_{1.35}$. A more detailed analysis of the phase diagram and the resulting Na_{Ru} off-stoichiometry can be found elsewhere[20].

The resulting mixture is milled for 60 min in a Spex 8000D Mixer/Mill using four 7.9 mm tungsten carbide balls. The reaction generates a substantial amount of heat, and precursor powders produced through milling are effectively amorphous. The resulting precursor powder is lightly ground in an agate mortar under argon, sieved through a 100 μm sieve and loaded into 2 ml CoorsTek alumina crucibles. Small quantities of precursor are also pressed into discs with a Carver press and subsequently buried in the precursor powder. Note that the unreacted powders are extremely hydroscopic and mildly pyrophoric, so the crucibles are sealed under approximately 1 bar of argon in fused silica ampoules and immediately placed within a preheated furnace at 900 °C. The samples are annealed for 30 min and are then immediately air-quenched before extracting powders within an argon glovebox with water and O_2 levels of <0.5 ppm. During annealing, both pellet and powder transform into the desired phase, whereas the pellet simultaneously densifies (sinters). This ensures that sample preparation is consistent throughout the measurement probes. The resulting powders are largely phase pure, with trace amounts of Ru metal (<1%) and Na_2CO_3 (<3%) due to an impurity in the starting Na_2O_2 reagent. Product powders are black and remain highly moisture sensitive.

$NaRhO_2$ powder was prepared and sintered as a phonon reference in heat capacity measurements for estimating the magnetic entropy. It was prepared following the methods reported elsewhere[44] and the phase purity was confirmed via X-ray diffraction (Supplementary Fig. 5).

X-ray synchrotron diffraction

High-resolution synchrotron powder diffraction data were collected using beamline 11-BM at the Advanced Photon Source, Argonne National Laboratory, using an average wavelength of 0.457925 Å. Both 300 and 5 K measurements were performed to check for any crystallographic phase transformations, as well as for a better analysis of the thermal parameters and occupancies at base temperatures. Discrete detectors covering an angular range from −6.000° to 16.000° in 2θ are scanned over a 34.000° range, with data points collected every 0.001° and a scan speed of 0.010° s^{-1}. Due to the air sensitivity of the materials, small quantities of $NaRuO_2$ were diluted with amorphous SiO_2 in a glovebox and sealed under argon in flame-tipped amorphous SiO_2 capillaries. These capillaries were nested within Kapton sleeves and held in place with a small amount of modelling clay. The resulting data and pattern refinement are shown in Supplementary Fig. 1 and the structural parameters are summarized in Supplementary Table 1. Diagnostic laboratory powder diffraction utilized a Panalytical Empyrean diffractometer (Cu Kα, 1.54 Å) in the Bragg–Brentano geometry.

Neutron diffraction

Neutron powder diffraction measurements were performed on the fixed-incident-energy triple-axis spectrometer HB-1A (λ = 2.37 Å) of the High Flux Isotope Reactor at Oak Ridge National Laboratory. Six grams of phase-pure polycrystalline $NaRuO_2$ was loaded in a cylindrical Cu can, which was then placed in a dilution insert of an orange cryostat, providing a base temperature of 50 mK. The collimation configuration of 40′-40′-40′-80′ yielded an energy resolution (full-width at half-maximum) at the elastic line of ~1 meV. The combination of the double-bounce monochromator system and the placement of the pyrolytic graphite crystal analyser for energy discrimination before the single He-3 detector provided an excellent signal-to-noise ratio. Additional contamination from higher-order wavelength contamination was minimized with the use of two pyrolytic graphite filters.

High-resolution neutron powder diffraction experiments were performed on the high-resolution neutron powder diffractometer BT-1 of the NIST Center for Neutron Research at the National Institute of Standards and Technology. A Ge(311) monochromator provided a λ = 2.0772 Å with the maximum neutron flux, allowing for full diffraction patterns to be collected in 12 h. Then, 4.5 g of phase-pure polycrystalline $NaRuO_2$ was loaded into a vanadium can under a helium atmosphere and placed into a top-loading flow-type orange cryostat, providing a base temperature of 1.6 K. Rietveld refinements of the neutron diffractograms were performed with TOPAS-Academic V6 with the results shown in Supplementary Table 1.

Inelastic neutron scattering

High-energy inelastic neutron scattering experiments were performed on the direct-geometry time-of-flight chopper spectrometer SEQUOIA at the Spallation Neutron Source at the Oak Ridge National Laboratory[45]. Then, 8 g of phase-pure polycrystalline $NaRuO_2$ was loaded in a cylindrical Al can that was placed in a top-loading helium cryostat, providing a base temperature of 1.8 K. Powder-averaged (Q, E) spectra were collected with incident energies of E_i = 80 and 42 meV, operating in the high-flux mode, providing an elastic resolution of ~7.8% and ~2.3% of E_i, respectively. Background contributions to the inelastic spectra were approximated by the measurement of an empty aluminium can, which was measured under identical experimental conditions for approximately one-third of the counting time allocated for the sample. Scattering maps (Fig. 3a,c) are temperature-subtracted data corrected for the Bose population factor obtained via $S(Q, E)_{sample,1.8K} - S(Q, E)_{can,1.8K} - A(E)(S(Q, E)_{sample,300K} - S(Q, E)_{can,300K})$, where $A(E)$ is the ratio of the Bose factors $A(E) = (1 - e^{-E/k_B T})_{T=1.8K}/(1 - e^{-E/k_B T})_{T=300.0K}$ for each E value. Cuts in Fig. 3b are cuts through the $(S(Q, E)_{sample} - S(Q, E)_{can})$ data at T = 1.8 K and T = 300.0 K.

Low-energy inelastic neutron scattering experiments were performed on the direct-geometry time-of-flight chopper spectrometer CNCS of the Spallation Neutron Source. Approximately 9 g $NaRuO_2$ was loaded under an inert atmosphere in a cylindrical Cu can that was placed on a HelioxVT A-100 mm ^{3}He insert in a top-loading 100 mm orange cryostat, providing a base temperature of 250 mK. Powder-averaged (Q, E) spectra were collected with incident energies of 3.32 and 1.55 meV, operating in the high-flux mode, providing an elastic resolution of 0.10 and 0.03 meV, respectively[46]. Background contributions to the inelastic spectra were approximated by an empty Cu can, which was measured under identical experimental conditions with equal counting times that were allocated for the sample and removed from the data. Normalization with a vanadium standard was performed to account for variations in the detector response and solid-angle coverage. Additional background subtracted maps of $S(Q, E)$ used for the scaling analysis data are presented in Supplementary Figs. 6 and 7.

Magnetic susceptibility

The temperature dependence of the zero-field-cooled (ZFC) and field-cooled d.c. magnetization of 17.6 mg $NaRuO_2$ powder placed in a brass holder was measured on a 7 T Quantum Design Magnetic Property Measurement System superconducting quantum interference device magnetometer. Data were continuously collected in the sweep mode with a ramp rate of 2 K min^{-1} in the presence of an external d.c. field of 1,000 Oe (1 Oe = (1,000/4π) A m^{-1}). The fit Pauli-like χ_0 was corrected for core diamagnetism (-53.8×10^{-6} emu mol^{-1} Oe^{-1}) (ref. 47).

Isothermal magnetization measurements of the same 17.6 mg $NaRuO_2$ sample at 1.8 K and 300.0 K were performed on a Quantum Design 14 T Dynacool Physical Property Measurement System (PPMS) employing the vibrating sample magnetometer option. ZFC data were continuously collected in the sweep mode with a ramp rate of 100 Oe s^{-1}.

The temperature dependence of the a.c. susceptibility of 10.1 mg $NaRuO_2$ powder was measured on a Quantum Design 14 T Dynacool PPMS employing the a.c. susceptibility option for the dilution refrigerator. A portion of a sintered pellet with approximate dimensions of 1.0 mm × 1.0 mm × 0.5 mm was adhered to a quartz sample mounting post with a thin layer of GE varnish. All the a.c. measurements were collected in the stable mode under ZFC conditions in an external d.c. magnetic field of 1 T and ramp rate of 0.08 K min^{-1}.

Heat capacity
The temperature and field dependence of the specific heat capacity of a 5.62 mg fragment of a phase-pure $NaRuO_2$ sintered pellet and 6.21 mg of its non-magnetic analogue $NaRhO_2$ were measured on a Quantum Design 14 T Dynacool PPMS employing the heat capacity option. Apiezon N grease was used to optimize thermal coupling between the sample and calorimeter stage. All the measurements were performed on heating, whereas all the measurements in the field were done under ZFC conditions. The phonon contribution was removed for estimating the magnetic entropy only, and this was achieved by the subtraction of a $NaRhO_2$ standard sample.

SPS
$NaRuO_2$ pellets (diameter, 10 mm; thickness, 2 mm) were prepared from phase-pure $NaRuO_2$ powder using field-assisted sintering (FCT Systeme). The pellets were pressed at 850 °C and 90 MPa for 60 min in an Ar-filled chamber with a pressure of 30 hPa, using a heating rate of 150 °C min^{-1} and cooling rate of 40 °C min^{-1}. All the pellets were subsequently ground to a 2,000 grit finish before resistivity measurements. Note that the SPS samples were primarily used to test the influence of grain-boundary effects by producing samples with a variety of experimental densities (Supplementary Fig. 4).

Resistivity
$NaRuO_2$ sintered pellets were sectioned into rectangular bars with approximate dimensions of 1.0 mm × 2.0 mm × 0.5 mm. Electrical contacts were made in the standard four-point geometry with contacts being made with a combination of gold wire and silver paint. The paint used was DuPont cp4929N-100, and the gold wire used for leads is Alfa Aesar 0.05 mm Premion 99.995%. Thermal contact and electrical isolation were ensured using layers of GE varnish and cigarette paper. The temperature dependence of electrical resistivity was measured with the electrical transport option on a 9 T Quantum Design Dynacool PPMS using a drive current of 10 µA and drive frequency of 100 Hz. Data were continuously collected in the sweep mode with a ramp rate of 2 K min^{-1}.

Muon spin relaxation measurements
The muon depolarization data were taken on the general-purpose surface muon spectrometer on the πM3.2 beamline at the Paul Scherrer Institute. For the zero-field data, the muon beam spin polarization was oriented at 45° to the muon momentum, whereas for the LF studies, the polarization was anti-parallel to the momentum. A pressed powder disc (diameter, 10 mm; thickness, 2 mm) was wrapped in thin Mylar foil and suspended in a gas-flow cryostat. Data were fit using the musrfit program[48] and the supporting fit parameters are presented in Supplementary Fig. 3.

Electronic structure calculations
First-principles electronic calculations based on density functional theory were performed using the Vienna ab initio simulation package (version 5.4.4)[49,50] with the LDA functional and projector-augmented wave pseudopotentials[51,52]. The plane-wave energy cutoff was set to 400 eV and a Γ-centred 15 × 15 × 15 k-point mesh was automatically generated within the Vienna ab initio simulation package. Initial biasing of spin polarization and tetrahedral smearing with Blöchl corrections were used for the self-consistent static calculation[53]. The electronic structure was calculated via a non-self-consistent run using the charge density from the static calculation with spin–orbit coupling and Hubbard U correction of 1 eV. A k-point path for the band structure calculation was generated using the AFLOW online tool[54]. All the calculations had energy convergence better than 10^{-6} eV.

Data availability
The data that support the findings of this study are available at https://doi.org/10.25349/D9R626.

References

44. Verger, L., Guignard, M. & Delmas, C. Sodium electrochemical deintercalation and intercalation in O3-NaRhO$_2$ and P2-Na$_x$RhO$_2$ layered oxides. *Inorg. Chem.* **58**, 2543–2549 (2019).
45. Granroth, G. E. et al. SEQUOIA: a newly operating chopper spectrometer at the SNS. *J. Phys.: Conf. Ser.* **251**, 012058 (2010).
46. Ehlers, G., Podlesnyak, A. A. & Kolesniko, A. I. The cold neutron chopper spectrometer at the Spallation Neutron Source—a review of the first 8 years of operation. *Rev. Sci. Instrum.* **87**, 093902 (2016).
47. Bain, G. A. & Berry, J. F. Diamagnetic corrections and Pascal's constants. *J. Chem. Educ.* **85**, 532 (2008).
48. Suter, A. & Wojek, B. M. Musrfit: a free platform-independent framework for µSR data analysis. *Phys. Procedia* **30**, 69–73 (2012).
49. Kresse, G. & Furthmüller, J. Efficient iterative schemes for ab initio total-energy calculations using a plane-wave basis set. *Phys. Rev. B* **54**, 11169 (1996).
50. Kressea, G. & Furthmüller, J. Efficiency of ab-initio total energy calculations for metals and semiconductors using a plane-wave basis set. *Comput. Mater. Sci.* **6**, 15–50 (1996).
51. Blöchl, P. E. Projector augmented-wave method. *Phys. Rev. B* **50**, 17953 (1994).
52. Kresse, G. & Joubert, D. From ultrasoft pseudopotentials to the projector augmented-wave method. *Phys. Rev. B* **59**, 1758 (1999).
53. Blöchl, P. E., Jepsen, O. & Andersen, O. K. Improved tetrahedron method for Brillouin-zone integrations. *Phys. Rev. B* **49**, 16223 (1994).
54. Setyawan, W. & Curtarolo, S. High-throughput electronic band structure calculations: challenges and tools. *Comput. Mater. Sci.* **49**, 299–312 (2010).

Acknowledgements

Technology for access to their neutron facilities. Certain commercial equipment, instruments or materials are identified in this document. Such identification does not imply recommendation or endorsement by the National Institute of Standards and Technology, nor does it imply that the products identified are necessarily the best available for the purpose.

Author contributions

Supplemental Information

Quantum Disordered Ground State in the Triangular Lattice Magnet NaRuO₂

Brenden R. Ortiz[1#], Paul Sarte[1#], Alon Hendler Avidor[1], Aurland Hay[1], Eric Kenney[2], Alexander I. Kolisneikov[3], Daniel M. Pajerowski[3], Adam A. Aczel[3], Keith M. Taddei[3], Craig M. Brown[4,5], Chennan Wang[6], Michael J. Graf[2], Ram Seshadri[1], Leon Balents[7], Stephen D. Wilson[1*]
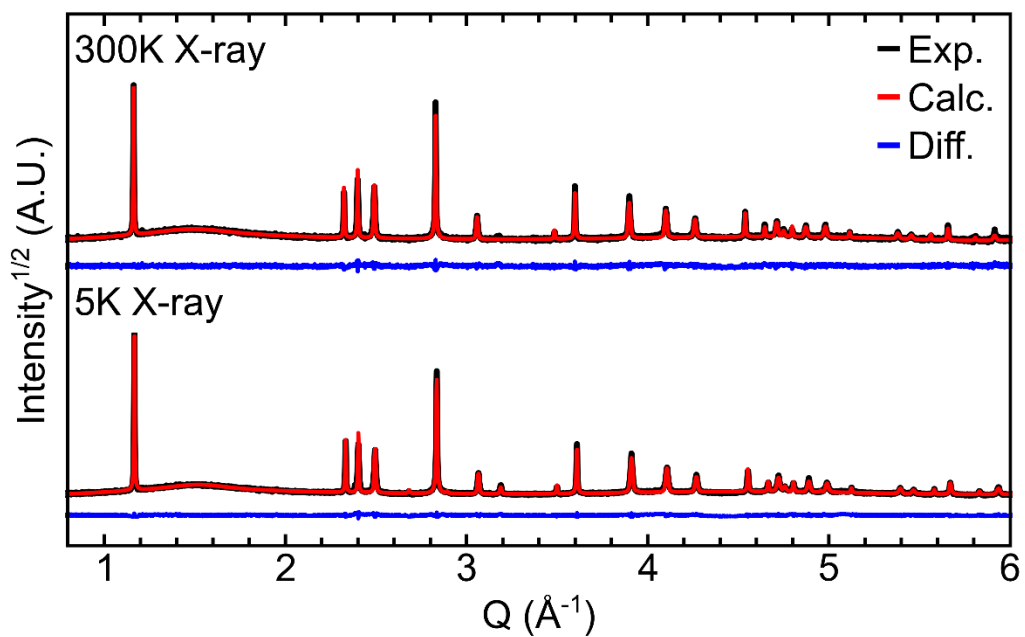
Supplemental Figure 1: X-ray diffraction data collected at 5 K and 300 K. Red lines show the output of the structural refinement model and blue lines denote the difference between the model and the data. Synchrotron x-ray data were collected at 11-BM at the Advanced Photon Source.

NaRuO$_2$ (BT1 300K)

a (Å)	c (Å)	V (Å^3)	c/a	α (°)
3.061039(82)	16.179435(467)	131.290(8)	5.29	94.7

site	x	y	z	Occ	B$_{eq}$
Ru	0	0	0.5	1.0	2.20(4)
Na	0	0	0	1.0	3.79(8)
O	0	0	0.23470(6)	1.0	1.75(3)

NaRuO$_2$ (BT1 1.5K)

a (Å)	c (Å)	V (Å^3)	c/a	α (°)
3.055783(95)	16.122636(506)	130.380(9)	5.28	94.8

site	x	y	z	Occ	B$_{eq}$
Ru	0	0	0.5	1.0	2.00(4)
Na	0	0	0	1.0	2.97(8)
O	0	0	0.23448(7)	1.0	1.52(4)

NaRuO$_2$ (APS 300K)

a (Å)	c (Å)	V (Å^3)	c/a	α (°)
3.065374(21)	16.228787(179)	132.064(2)	5.29	93.7

site	x	y	z	Occ	B$_{eq}$
Ru	0	0	0.5	1.0	2.31(5)
Na	0	0	0	1.0	3.68(9)
O	0	0	0.23641(42)	1.0	1.79(9)

NaRuO$_2$ (APS 5K)

a (Å)	c (Å)	V (Å^3)	c/a	α (°)
3.060344(13)	16.162925(101)	131.096(1)	5.28	95.2

| site	x	y	z	Occ	B$_{eq}$
Ru	0	0	0.5	1.0	2.01(2)
Na	0	0	0	1.0	3.16(5)
O	0	0	0.23365(17)	1.0	1.84(9)

Supplemental Table 1: Crystallographic parameters for NaRuO$_2$ using both neutron and synchrotron diffraction data. Occupancy values refine to within unity and were fixed for later analysis. For synchrotron data, the B$_{eq}$ for oxygen was constrained near that of the neutron data. Values in parenthesis are one standard deviation. Refinement GOF is between 1.8-1.9 for all refinements.
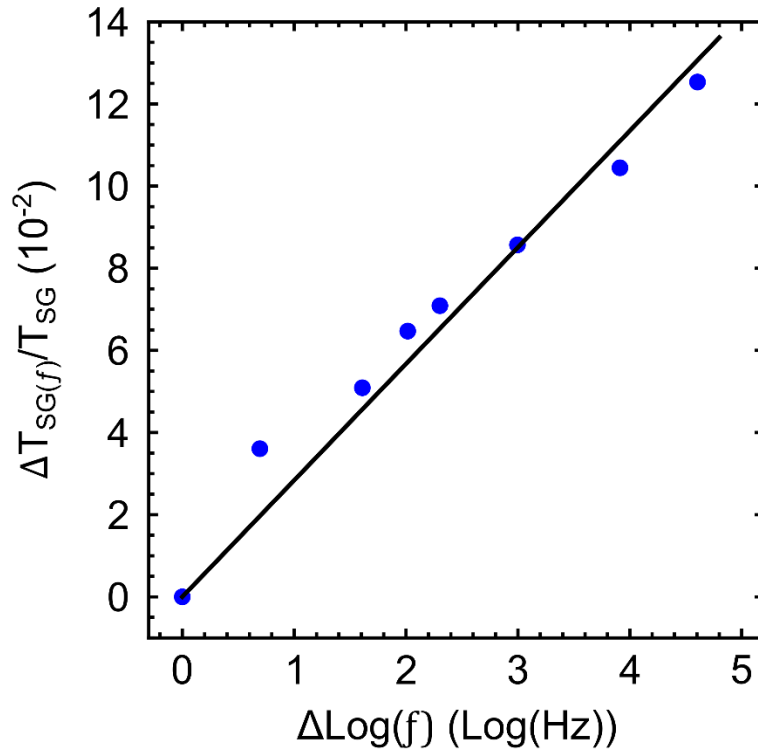
Supplemental Figure 2: Frequency dependence of the low-temperature cusp in the AC susceptibility of NaRuO$_2$. The resulting Mydosh parameter $K = \frac{\Delta T_f}{T_f \log(\Delta f)} = 0.028$ is an unusual intermediate value. It is significantly smaller than that expected for a superparamagnet and significantly larger than that expected for a conventional spin glass.[1,2,3] This weak freezing represents a small amount of entropy and marks a crossover into a state with persistent spin fluctuations as described in the main text of the manuscript.
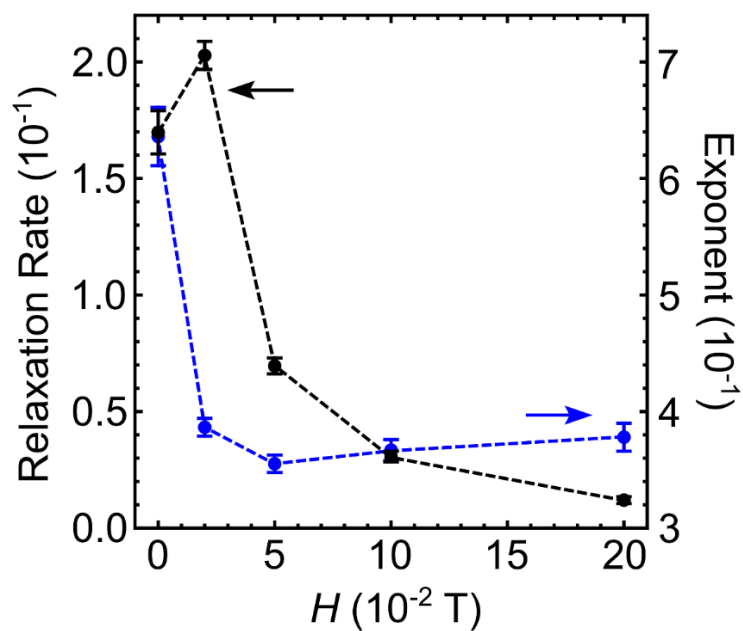
Supplemental Figure 3: Fit parameters resulting from the model of the longitudinal field muon spin polarization data at 1.5 K where the polarization is parameterized by the form $P(t) = GbG(\Delta; R; t)e^{(-\lambda_{GbG}t)^{\beta}}$. The relaxation rate λ_{GBG} (left axis) and stretched exponent β (right axis) are plotted as a function of the applied longitudinal magnetic field. Error bars represent one standard deviation in the parameters derived from nonlinear least square fits to the data.
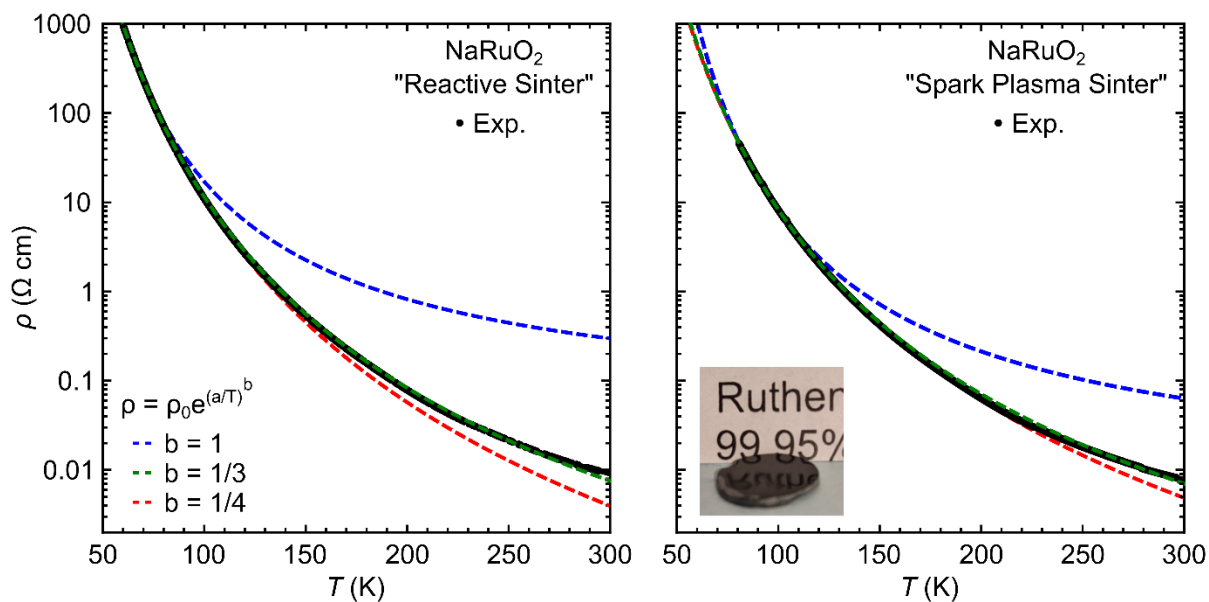
Supplemental Figure 4: Comparison of electrical transport data between the samples prepared via a cold-press plus reactive sinter as presented in the main text and via spark plasma sintering (SPS) which provides an even higher pellet density. The left panel shows temperature dependent resistivity from a reactive sinter sample while the right panel shows the results from the SPS sample. The inset shows a mirror surface finish once polished, demonstrating the high density of the sample. Dashed lines are fits to the transport models described in the main text.
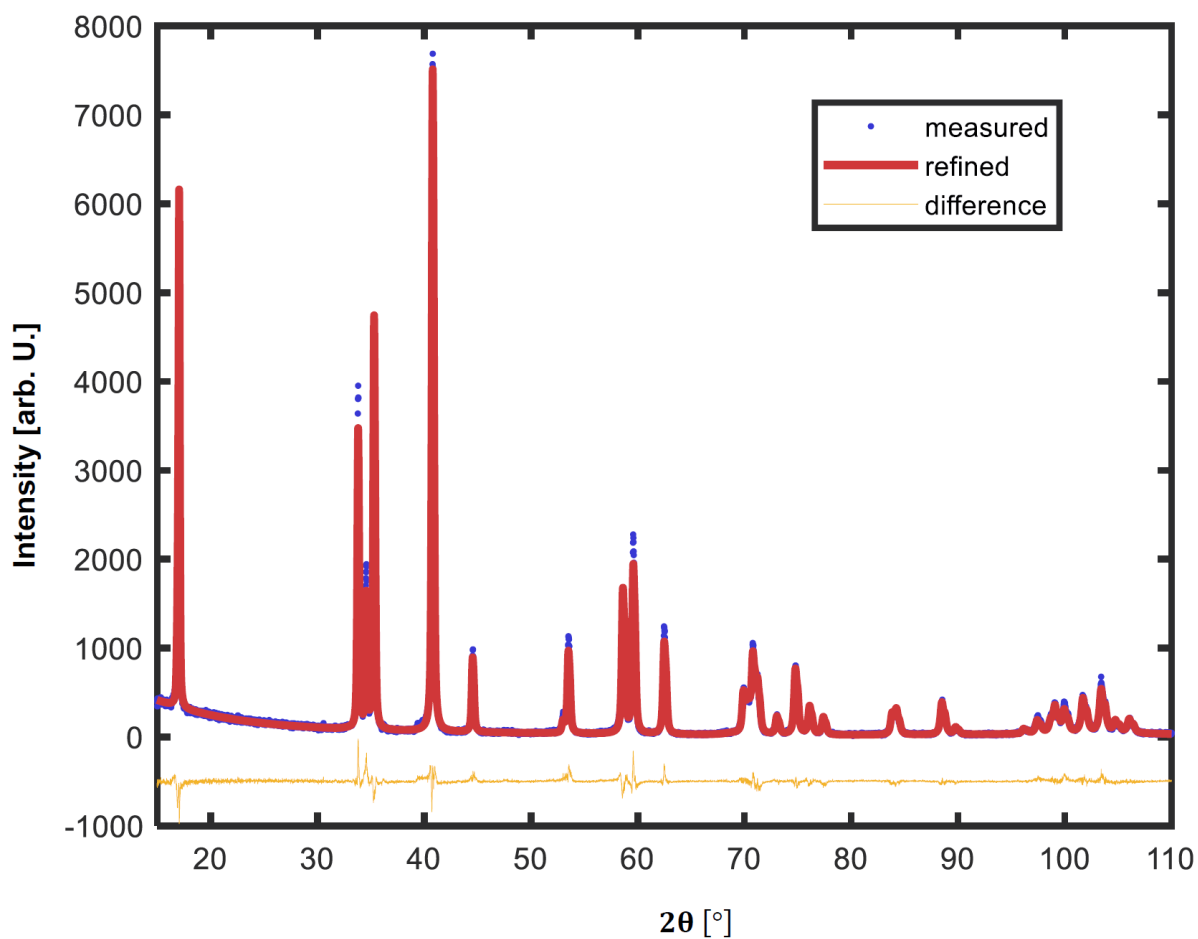
Supplemental Figure 5: NaRhO$_2$ x-ray powder diffraction data characterizing the phase purity of powder used as a phonon reference for magnetic entropy calculations. The red line shows the results of Rietveld refinement of the powder pattern and the yellow line shows the difference between the data and the Rietveld model. Data were collected using a Panalytical Empyrean diffractometer (Cu Kα, 1.54 Å) in the Bragg-Brentano geometry
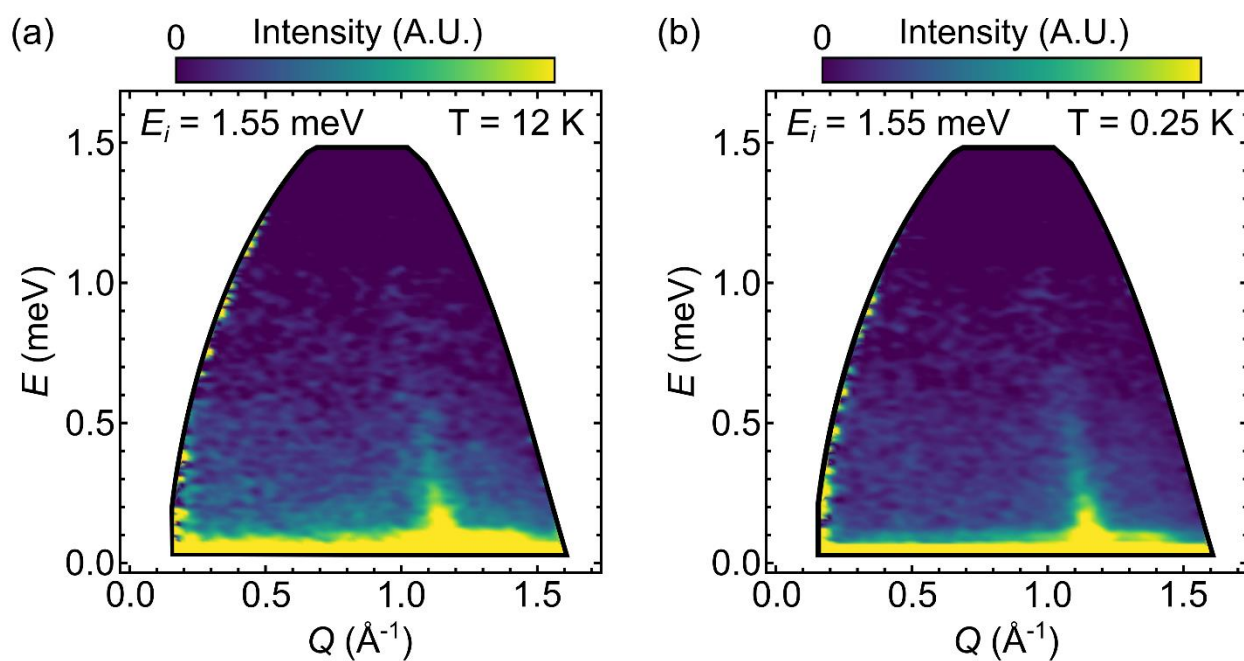
Supplemental Figure 6: Momentum and energy maps of neutron scattering $I(Q,\omega)$ collected at (a) 250 mK and (b) 12 K with an incident energy E_i=1.55 meV on $NaRuO_2$ powder as described in the main text. The narrow, slightly sloping tail centered near Q=1.2 Å^{-1} arises from the CNCS resolution ellipsoid catching portion of the nuclear Bragg peak and quasielastic scattering.
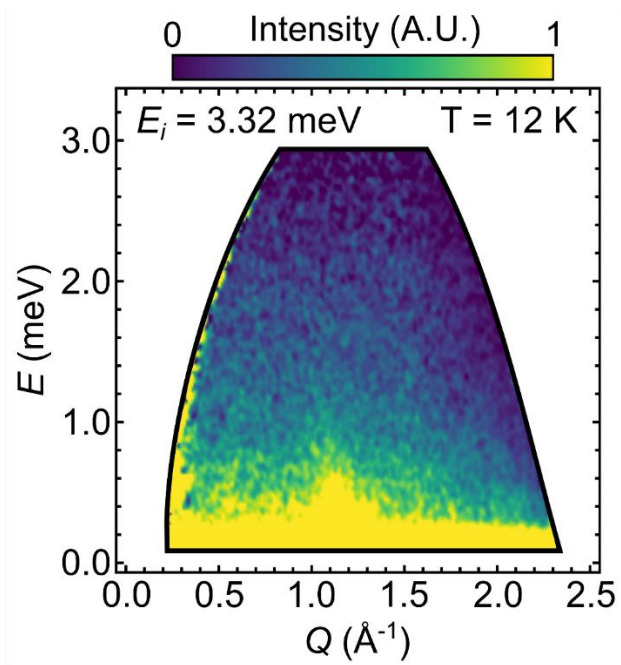
Supplemental Figure 7: Momentum and energy map of neutron scattering $I(Q,\omega)$ collected at 12 K with an incident energy E_i=3.32 meV on NaRuO$_2$ powder as described in the main text.
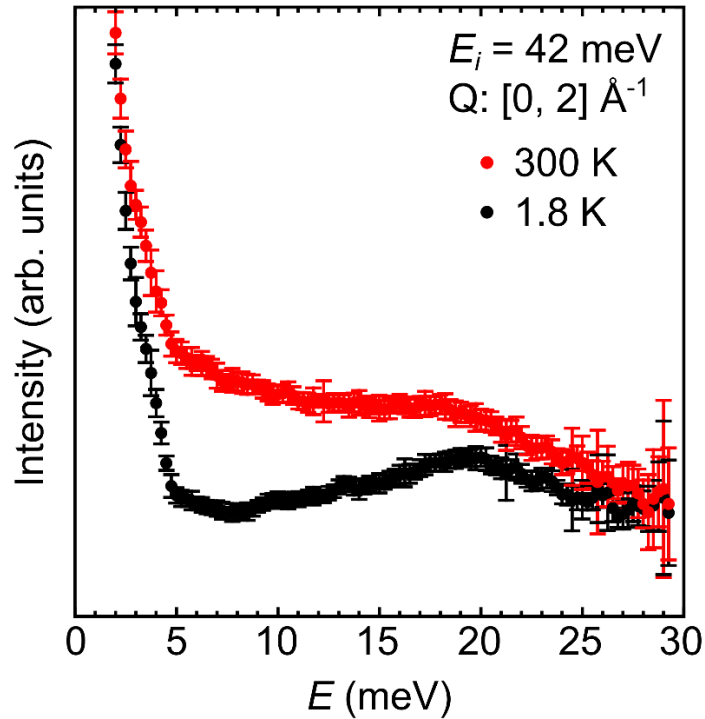
Supplemental Figure 8: Momentum-averaged cut through scattering $S(Q,\omega)$ collected at 1.8 K and 300K with an incident energy E_i=42 meV on $NaRuO_2$ powder as described in the main text. Error bars in all panels represent one standard deviation in the data based on Poissonian statistics with the sample size being the neutron counts.

References:

[1] H D Zhou, C R Wiebe, A Harter, N S Dalal, and J S Gardner "Unconventional spin glass behavior in the cubic pyrochlore $Mn_2Sb_2O_7$" J. Phys.: Condens. Matter 20, 325201 (2008).

[2] Johannes Kroder, Johannes Gooth, Walter Schnelle, Gerhard H. Fecher, and Claudia Felser "Observation of spin glass behavior in chiral $Mn_{48}Fe_{34}Si_{18}$ with a β-Mn related structure" AIP Advances 9, 055327 (2019).

[3] J. A. Mydosh Spin Glasses: An Experimental Introduction (1993).